applied sciences

MDPI

Article

Reproducibility Assessment of Zirconia-Based Ceramics Fabricated out of Nanopowders by Electroconsolidation Method

Miroslaw Rucki [1,*], Edvin Hevorkian [2], Jolanta Natalia Latosińska [3], Vasyl Kolodnitskyi [4], Leszek Chalko [2], Dmitrij Morozow [2], Waldemar Samociuk [5,*], Jonas Matijosius [1], Milan Masař [6] and Tomasz Ryba [2]

1 Institute of Mechanical Science, Vilnius Gediminas Technical University, Sauletekio al. 11, LT-10223 Vilnius, Lithuania
2 Faculty of Mechanical Engineering, Casimir Pulaski Radom University, Stasieckiego 54, 26-600 Radom, Poland
3 Faculty of Physics and Astronomy, Adam Mickiewicz University, Uniwersytetu Poznańskiego 2, 61-614 Poznań, Poland; jolanta.latosinska@amu.edu.pl
4 V. Bakul Institute for Superhard Materials, National Academy of Science of Ukraine, Avtozavodska Str. 2, 04074 Kyiv, Ukraine
5 Faculty of Production Engineering, University of Life Sciences in Lublin, Gleboka 28, 20-612 Lublin, Poland
6 Center of Polymer Systems, Tomas Bata University in Zlin, Trida Tomase Bati 5678, 76001 Zlin, Czech Republic; masar@utb.cz
* Correspondence: m.rucki@urad.edu.pl (M.R.); waldemar.samociuk@up.lublin.pl (W.S.)

Featured Application: the results of this work can be useful in any application of zirconia-based ceramics, especially when considering various sintering methods.

Abstract: The repeatability of the material properties is required to ensure the proper performance of the engineered systems that are constructed using these materials. In this paper, an analysis of the sintered ceria-stabilized zirconia is presented. This material exhibited high mechanical properties, due to the mechanism of strengthening via phase transition. The reproducibility was assessed for the material made out of a starting powder produced by fluoride salt precipitation. To fabricate specimens, a novel electroconsolidation method was used, ensuring a high heating rate, relatively low sintering temperatures, and short holding time. Weibull analysis was performed considering the bending strength of specimens and their microhardness. The obtained values of both shape parameter m and scale parameter σ_0 indicated that the ZrO_2 stabilized with 5 wt.% CeO_2 samples exhibited low variability of strength and hardness. The experimental evidence and statistical analysis reveal an influence of the m-phase, which has lower symmetry and therefore its addition makes ceramic weaker and softer. Furthermore, its progressive replacement by the t-phase, which has higher symmetry, makes ceramic both harder and stronger. Reducing the mol% increases the risk of the appearance of the highest addition of the monoclinic phase; increasing it is unfavorable from the point of view of the sintering process. Statistical and manufacturing evidence suggests that the choice of 5%/mol is optimal.

Keywords: sintering; electroconsolidation; zirconia; repeatability; Weibull distribution

Academic Editor: Ephraim Suhir

Received: 7 April 2025
Revised: 24 April 2025
Accepted: 27 April 2025
Published: 30 April 2025

Citation: Rucki, M.; Hevorkian, E.; Latosińska, J.N.; Kolodnitskyi, V.; Chalko, L.; Morozow, D.; Samociuk, W.; Matijosius, J.; Masař, M.; Ryba, T. Reproducibility Assessment of Zirconia-Based Ceramics Fabricated out of Nanopowders by Electroconsolidation Method. *Appl. Sci.* **2025**, *15*, 4955. https://doi.org/10.3390/app15094955

1. Introduction

Ceramic materials based on zirconia (zirconium oxide, ZrO_2) attract the attention of researchers and industry due to their unique physical and chemical properties, such as high flexural strength, hardness, corrosion resistance, and thermal stability [1]. Due to these advantageous properties, zirconia is considered one of the vital materials for engineering, tools, dental, or orthopedic applications [2–4]. Zirconia-based ceramics serve as a catalyst

and are used as a material for solid fuel cells due to their unique characteristics [5]. Zirconia exhibits superior thermal resistance with a melting temperature ca. 2700 °C, which makes it a more effective material for isolation layers than glass or quartz fibers [6].

Pure zirconia, under low-pressure conditions, exists in three distinct crystalline phases: monoclinic (m-ZrO_2, P21c, stable to 1170 °C), tetragonal (t-ZrO_2, P42/nmc, stable 1170–2370 °C) and cubic (c-ZrO_2, Fm3m, stable 2370–2900 °C). In the presence of pressure, a primary phase transition from monoclinic to orthorhombic phase is observed at 3–11 GPa [7–9] (brookit phase, either Pbcm or Pbca), with a secondary transition occurring at 9–15 GPa [8] (Pnam, isostructural to cotunnite). The rutile phase, which is theoretically predicted and should be more stable than the monoclinic phase, has not yet been observed in experimental studies. Furthermore, zirconia has a polycrystalline biphasic structure [10]. At elevated temperatures, pure zirconia has a tetragonal structure *t*-ZrO_2, and a monoclinic phase *m*-ZrO_2 at room temperature, but two phases, t-ZrO_2 and m-ZrO_2, can coexist, e.g., in a matrix. Since the tetragonal phase is unstable, it is usually stabilized with yttria, making up a hard, tough structural ceramic feasible for the high-temperature applications, e.g., in jet engines [11]. Recently, cerium has been considered as an attractive alternative to yttria for stabilizing zirconia, due to its higher toughness compared with yttria-stabilized zirconia, even though CeO_2 ceramics exhibited relatively low strength [12]. Some researchers pointed out that zirconia with Y_2O_3 has better mechanical properties, but it suffers from the disadvantage of degrading at low temperature. Experimental evidence suggests that CeO_2-doped zirconia is more stable [13]. Due to higher mobility of grain boundaries, the grain size after sintering is larger, making challenging the fabrication of completely dense ceria-stabilized zirconia ceramics with fine grains [14].

In recent years, significant attention has been paid to nanostructured ceramics, because reducing the grain size results in increased hardness and fracture resistance of the ceramic. Indeed, the ZrO_2 nanopowders exhibit enhanced mechanical and functional characteristics compared to coarse-grained materials [15]. One of the most promising methods for obtaining such nanopowders is an electrospray deposition technique [16]. However, for successful industrial application, it is necessary to ensure the reproducibility of the properties of the obtained materials. It is widely known that the particle size distribution of the initial powder plays a crucial role in further compaction and thus has an effect on the properties of the sintered material [17]. The utilization of nanopowders is contingent upon the procurement of substantial quantities of materials that are characterized by their reproducible quality.

Research has demonstrated that by optimizing the conditions of electrospray deposition, high reproducibility of the structure and properties of nanopowders can be achieved [18]. In particular, under certain process parameters, it is possible to obtain particles with a narrow size distribution, ensuring stable mechanical properties of the sintered ceramic products. Controlling the phase composition is an important factor, as well, since the presence of different phases (tetragonal, monoclinic, cubic) affects the mechanical properties and stability of the material. Optimization can be performed by minimizing or maximizing some objective functions, such as stiffness, mass, etc. [19].

Similarly, it is crucial to keep repeatable processing conditions to fabricate sintered ceramics with reproducible properties [20]. However, on the microscopic scale, random variation in strength may occur due to the randomly distributed microdefects that are common in quasi-brittle materials in terms of spatial arrangement, orientation, size, and shape [21]. Thus, it is convenient to estimate the likelihood of the crack propagation as a measure of the material's fracture resistance.

Weibull analysis (WA) is a statistical analysis widely used in reliability applications to identify failure modes [22,23]. It is an effective technique for obtaining material reliability

results at a moderately low rate, with the reliability of the material or component being assured [24]. The Weibull modulus of aggregate tensile strength distribution is correlated to the heterogeneity of particle binding force distribution within the aggregate. The sensitivity of the Weibull modulus to detect small differences in the internal structure of aggregates depends on the standardization of aggregate shape and sphericity. The Weibull modulus is highly sensitive to the heterogeneity of particle binding force distribution within the aggregate. An increase in the heterogeneity of the particle binding force distribution results in a linear decrease in the Weibull modulus of the aggregate tensile strength [25]. The two-parameter (2P) Weibull distribution function, based on scale and shape parameters, is the most commonly used statistical model for characterizing the strength of modern ceramics [26]. The primary benefit of Weibull analysis is that it facilitates the analysis of failures, even with limited data samples. It also provides a graphical representation of the individual failure modes that can be readily interpreted, as well as an indication of the failure physics (based on the slope of the distribution).

The probabilistic strength description parameters obtained from the Weibull distribution should match the observed material microstructure. Indeed, the Weibull distribution has been successfully used to describe the fracture strength of microscale materials such as silicon and composite-reinforcing fibers and has been used to a lesser extent for thin films, nanotubes/wires, and 2D materials [27].

The Weibull distribution has been extensively utilized in the fields of reliability analysis and durability testing of a wide range of industrial products. This distribution has been found to provide an effective representation of the degradation trajectory or the form of material failure. Additionally, it has been demonstrated to assist in addressing the challenges posed by uncertainty and randomness in damage caused by internal defects in brittle materials [28].

Despite significant success reported on the zirconia ceramics research, the mechanisms of its performance are not yet fully established. For instance, it is necessary to ascertain the details of the microstructural transformation and stability-dependent factors of *t*:*m* phase proportions, surface chemistry, and porosity, as well as properties dependent on the applied load. The research described in this paper contributes to fill some of these gaps. The reproducibility of the properties of ceramics sintered out of ZrO_2 nanopowders obtained by electrospray deposition is a key factor for the successful improvement of the electroconsolidation device prototype, designed for further investigations. The objective of this paper was to analyze the distribution of properties, both for synthesis and processing parameters, using the Weibull model. The powder characteristics, a description of the sintering process, results of strength and hardness measurements, and most importantly, their statistical analysis enabled an assessment of the degree of material reproducibility.

2. Materials and Methods

2.1. Powder Preparation

The synthesis of zirconium nanopowders was accomplished through the utilization of the fluoride salt decomposition method, a process that has been extensively delineated in [29]. However, the precipitation process was performed at three different temperatures, 20 °C, 50 °C, and 80 °C, and the ratio of metallic zirconium to polyvinyl alcohol (PVC) was varied, as follows: m(Zr):m(PVC) was 1:0.1, 1:0.5, and 1:1.

The as-obtained substance was filtered and washed using distilled water, and then it was dried for 48 h at 20 °C. Then, the powder was heated up to 800 °C, applying the heating rate ca. 100 °C/h, and held for 4 h. Afterwards, the zirconia powder was cooled down to room temperature. To obtain homogeneity of the nanopowder, it was mixed with

the planetary micro mill Pulverisette 7 (Fritsch GmbH, Idar-Oberstein, Germany), shown in Figure 1.

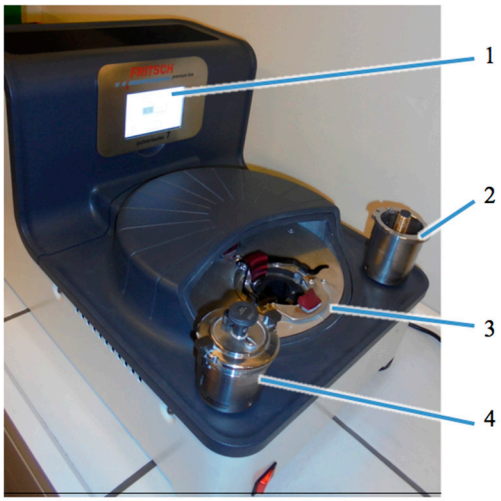

Figure 1. Planetary micro mill Pulverisette 7 used in the research. 1—Screen, 2—Counterweight, 3—Supporting disc, 4—Grinding bowl.

The use of cerium oxide was instrumental in the stabilization of the zirconium powder. Nanopowder CeO_2 was purchased from Nanografi Nano Technology (Ankara, Turkey). It was gradually added to the blend and mixed until homogeneity. The amount of added cerium oxide was calculated to obtain 5 mol% proportion in the zirconia powder. The blend was prepared by dry method and with application of isopropyl alcohol. The mixing process lasted for 2 h with planetary disk rotational speed of 160 rpm.

The degree of stabilization is dependent on the particular stabilizer type, its calcination temperature, and quantity of contaminations [30]. The reports on Ce-stabilized zirconia with CeO_2 content from 8 mol% up to 16 mol% pointed out the poor sinterability of these materials that required a prolonged heating, which, in turn, resulted in higher grain growth [31]. Thus, it was decided to perform experiments with a reduced ceria proportion of 5 mol%. It was also noted that during the synthesis process, this composition exhibited higher thermodynamic stability and lower structural anisotropy.

2.2. Electroconsolidation Method

A method for fabrication of sintered specimens was a sort of powder metallurgy technique, a modified spark plasma sintering (SPS) [32], or electric field activated sintering technology (E-FAST) [33] method. The main idea and apparatus used for electroconsolidation are presented in detail elsewhere [34]. The sole source of heat in this modified SPS process was high electrical current, reaching ca. 5000 A. Unlike a typical SPS pulsed direct current [35], an alternating current is used in the electroconsolidation technique.

The electroconsolidation apparatus is shown in Figure 2. Figure 2a presents the device, specifying its main units. In Figure 2b, graphite mold is presented, shaped for the fabrication of cylindrical specimens of diameter 11 mm and height 5 mm.

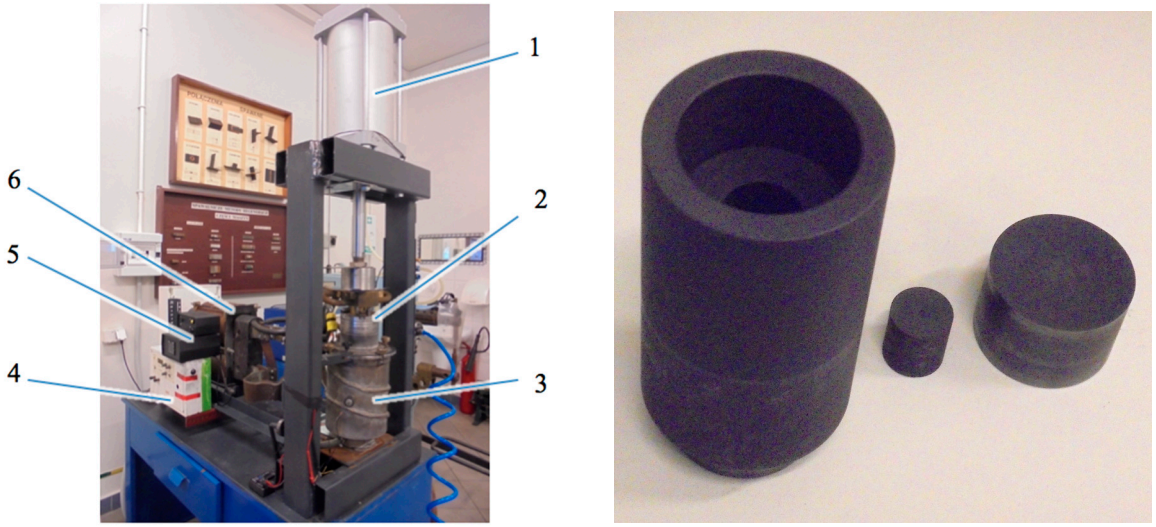

(**a**) (**b**)

Figure 2. Electroconsolidation apparatus: (**a**) Overall view; (**b**) Disassembled graphite mold. 1—Pressing unit, 2—Built-in mold, 3—Vacuum chamber, 4—Electrical current filter, 5—Temperature control unit, 6—Current transformer.

The synthesized nanopowders ZrO_2–5 wt.% CeO_2 were sintered at temperature 1400 °C under mechanical pressure 45 MPa; holding time was 2 min.

2.3. Materials Characterization

Scanning electron microscopy (SEM) was utilized for the purpose of sample analysis. It provides information about the surface topography and composition of the sample. The experimental procedure was performed using NovaNanoSEM 450 microscope (FEI Europe B.V., Eindhoven, The Netherland). Microscopic images were taken using the following detectors: TLD (Through the Lens Detector, topographic contrast) and CBS (Circular Backscatter Detector, material contrast) at accelerating voltages of 5 kV and 15 kV, respectively. Distance to sample (Working Distance, WD) was 4 mm for TLD detector and 5 mm for CBS.

To determine the specific surface area of the initial powders, the BET (Brunauer–Emmett–Teller) method was used, with nitrogen (N_2) being the widely accepted standard adsorptive [36]. For that purpose, the device BELSORP-mini II produced by BEL Japan, Inc. (Toyonaka, Japan) was employed. All samples were measured by degassing at 100 °C for 3 h.

The elemental microanalysis was performed using Octane energy dispersive X-ray detector (AMETEK, Inc., Berwyn, PA, USA). The applied Octane Elect Plus silicon drift detector (SDD) was equipped with a chip of 30 mm^2 area. The X-ray diffraction analysis (XRD) was performed using Philips X'Pert Pro Materials Powder Diffractometer (Philips Analytical, now PANalytical, Almelo, The Netherlands) in order to evaluate the phase composition of the zirconia powder. The CuKα radiation source was used in XRD, with an anode voltage of 45 kV and a current of 40 mA.

The strength analysis was based on the results of three-point bending strength tests and Vickers hardness measurements. For that purpose, Bending Testing Machine DELTA 5–200 was used (Form+Test Seidner&Co. GmbH, Riedlingen, Germany). For the hardness, the tester type FALCON 400G2 produced by Innovatest (Maastricht, The Netherland) was applied.

2.4. Weibull Analysis

To ascertain the reliability of the samples, a Weibull analysis was undertaken. The Weibull distribution is a type of statistical continuous probability distribution; a flexible model that is frequently used to approximate the normal, Rayleigh, or exponential distribution. It can be used to model data exhibiting right-skewed, left-skewed, or symmetric properties.

This versatility renders it a suitable model for assessing reliability. The Weibull distribution has been demonstrated to be an effective extreme value distribution for the purpose of predicting the occurrence of extreme phenomena. Therefore, it is widely used to describe the probabilistic failure behavior of materials. In general, the Weibull distribution is defined either by its probability density function or cumulative distribution function. The original Weibull model is three-parametric with shape indicating whether the failure rate is increasing, decreasing, or constant over time, scale that stretches or compresses the distribution, and threshold that shifts the distribution along the X-axis. The latter is optional and neglected in the 2D model. The parameters of the Weibull distribution can be determined analytically, employing either least squares (rank linear or non-linear regression) or maximum likelihood estimation (MLE). In this study, the former approach was used.

Thanks to linearization procedure, the Weibull method can theoretically work with extremely small samples, even with two or three failures. In order to achieve statistical relevance, it is necessary to increase the size of the sample. Usually, Weibull analysis requires at least 30 samples (the central limit theorem requirement). For a distribution that differs significantly from normal, it may be necessary to use as many as about 30 samples. However, it is important to note that, given the wide array of probability distributions that exist, this criterion may not be universally applicable. Therefore, this rule can be revised under certain prerequisites [37,38].

However, relatively small dispersion of the values was noted, so based on [39], it was found acceptable to reduce the number of samples down to 15. The performed Shapiro–Wilk test did not show a significant departure from normality, with parameters $W(15) = 0.9445$, $p = 0.4428$ for bending strength and $W(15) = 0.9447$, $p = 0.4455$ for hardness. Since p-values in both cases were larger than α, we accepted the H_0 hypothesis, assuming that the data were normally distributed.

3. Results and Discussion

3.1. Characterization of the Initial Powder

The powder synthesized via the precipitation route described in Section 2.1 is shown in Figure 3. In particular, the SEM image is presented in Figure 3a, and the XRD diagram is provided in Figure 3b.

The homogeneity of powder morphology can be noted from the SEM image (Figure 3a). It can be expected that the highly uniform particle size distribution contributed to the improved sinterability of the zirconia powder. The XRD diagram (Figure 3b) exhibits the presence of both phases, tetragonal t-ZrO_2 and monoclinic m-ZrO_2. Thus, the sample under investigation exhibits a biphasic structure.

Figure 4 shows the BET (Brunauer–Emmett–Teller) isotherm of the initial powder. Its specific surface area a_{sBET} was found to be 6.3. Compared to the powder obtained by other means, this powder was of significantly higher quality. The specific surface area for the second powdered sample was $a_{sBET} = 3.7$, and this powder was of poor quality and thus excluded from further studies.

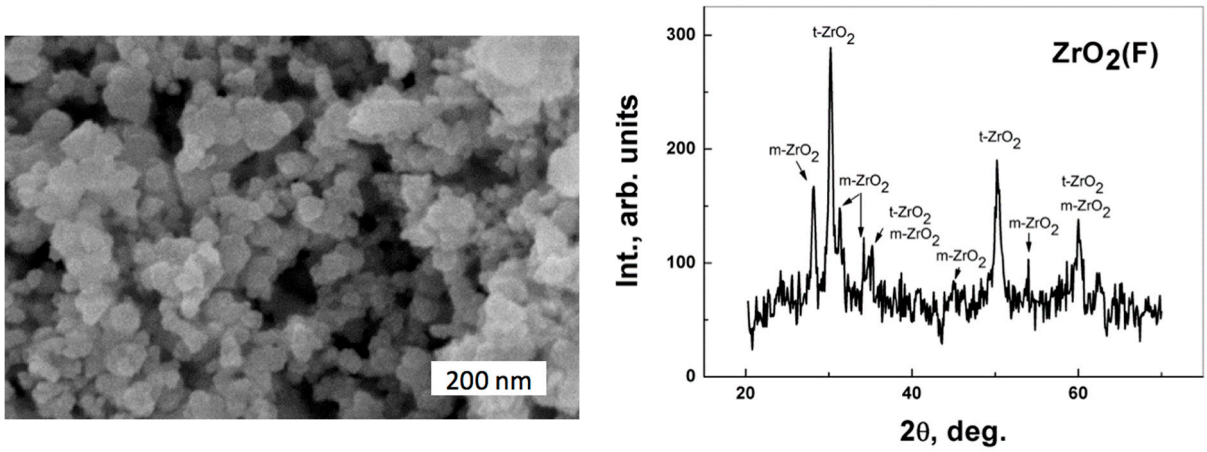

(**a**) (**b**)

Figure 3. The synthesized nanopowder ZrO_2 stabilized with 5 wt.% CeO_2: (**a**) SEM image; (**b**) XRD diagram specifying tetragonal *t*-ZrO_2 and monoclinic *m*-ZrO_2 phases.

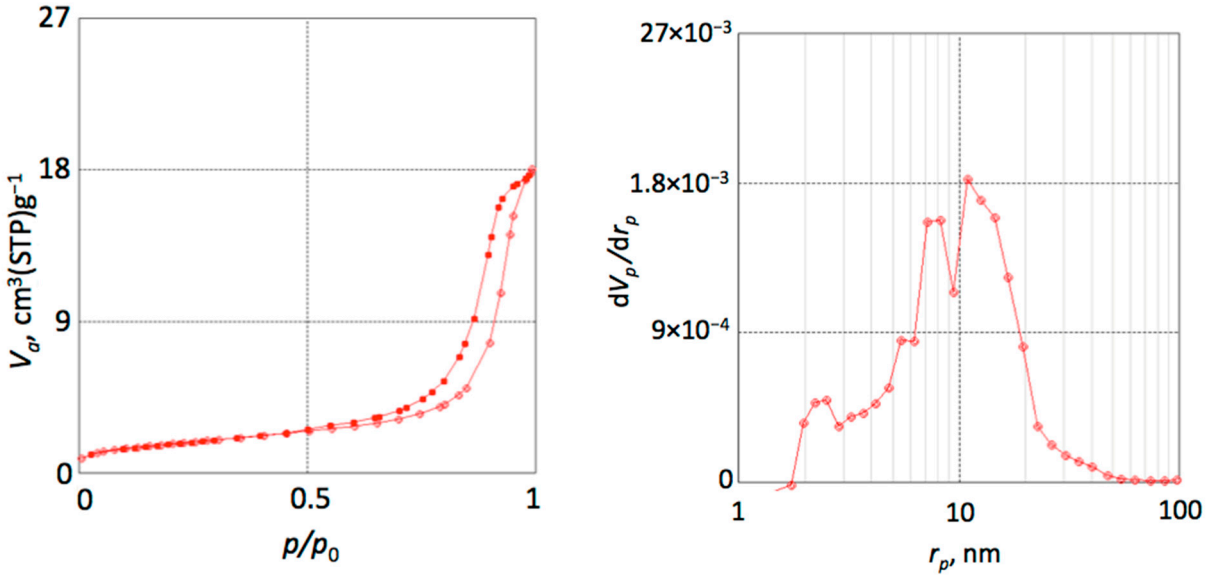

(**a**) (**b**)

Figure 4. The BET isotherm for the synthesized nanopowder ZrO_2 stabilized with 5 wt.% CeO_2: (**a**) BET (Brunauer–Emmett–Teller) isotherm hysteresis; (**b**) diagram of differential dV_p/dr_p.

The hysteresis shown in Figure 4a belongs to a Type IVa isotherm, according to the classification provided in [40]. Its two branches represent adsorption and desorption associated with capillary condensation. Capillary condensation typically occurs in granular or porous media and can strongly alter the properties of the materials. Its presence suggests the van der Waals interactions between the molecules assemble crystals to create atomic-scale capillaries in the condensed state.

Although the final saturation plateau is very small, this indicates a mesoporous material. The increase in mesoporosity can be attributable to the augmented number of grain boundaries, consequent to the formation of phase-separated nanocomposites.

For nitrogen, adsorption took place in cylindrical pores at 77 K, and hysteresis started to occur for pores above 4 nm in width. The pore volume versus pore diameter shown in Figure 4b reveals three local extremes at diameter values of about 2.5, 7.5, and 11 nm.

The observed morphology and the results of the BET analysis indicated that the initial powder exhibited good sinterability.

3.2. Microstructural Analysis of the Sintered Specimens

The microstructure of a sintered sample is shown in Figure 5. The structure of the specimen was found to be homogeneous with several small dark inclusions of distinguishable size. The three areas selected for the elemental analysis are illustrated in Figure 5b, and the numerical data are listed in Table 1.

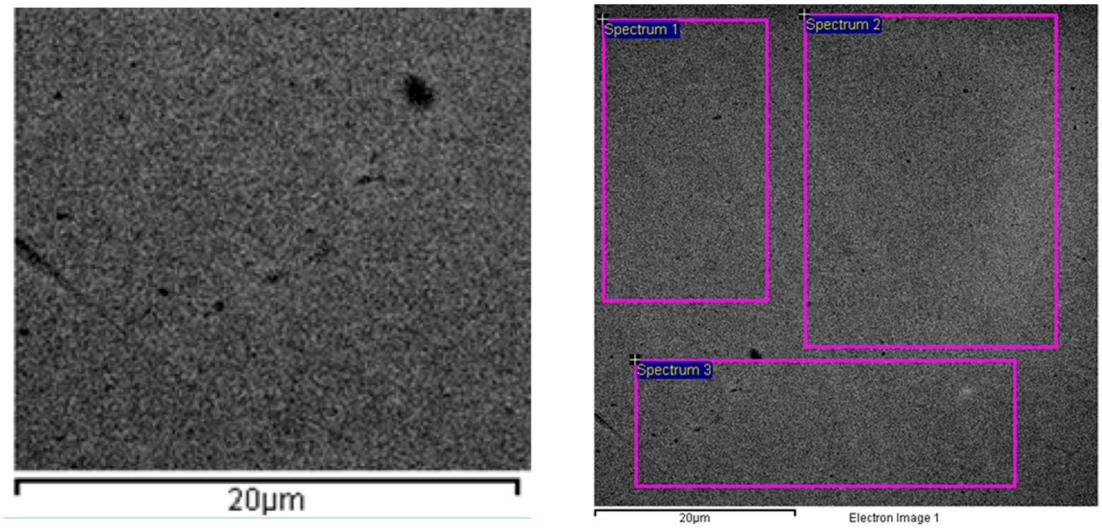

(**a**) (**b**)

Figure 5. The sintered specimen ZrO_2 stabilized with 5 wt.% CeO_2: (**a**) Microstructure; (**b**) Spectra areas for elemental analysis.

Table 1. Elemental analysis of sintered ZrO_2–5wt.% CeO_2 specimen.

Spectrum No.	O, wt.%	Ce, wt.%	Zr, wt.%
Spectrum 1	30.5	5.39	64.1
Spectrum 2	30.8	4.99	64.2
Spectrum 3	31.9	4.27	64.8

The data in Table 1 suggest that some non-uniformity of ceria distribution in the zirconia matrix took place. However, its scale does not threaten the strength characteristics of the sintered material. From the perspective of fracture toughness, the proportion of tetragonal to monoclinic zirconia appeared more important. Overall, the *t*-ZrO_2 phase constituted ca. 95%, while the content *m*-ZrO_2 phase was ca. 5% in the sintered specimen. An increase in the monoclinic phase content upon cooling of zirconia sintered at temperatures higher than 1400 °C was reported in [41], which should not be expected in the present experiments with the zirconia sintered at 1400 °C. Thus, the negative effect of the monoclinic phase could be considered negligible.

The presence of the different phases (i.e., monoclinic, tetrahedral, and cubic) is evidenced in the experimental studies. The histogram shown in Figure 6 provides a concise overview of these data. The horizontal axis shows the mol% value, while the *Y*-axis is utilized to demonstrate the number of mentions of these structures in the literature.

When the mol% of CeO_2 in a given composite falls between 10% and 80%, the existence of the composite in various phases has been reported. The higher CeO_2 content, the higher the symmetry (for mol% < 8% formulation, it is typically monoclinic, 8 < mol% < 75% tetrahedral, or cubic and mol% > 75% cubic). The nanopowders with mol% equal to 10, 25, 50, and 75% exhibit tetrahedral symmetry, while with mol% equal to 90% exhibits cubic symmetry. Consequently, elevated mol% is associated with higher symmetry.

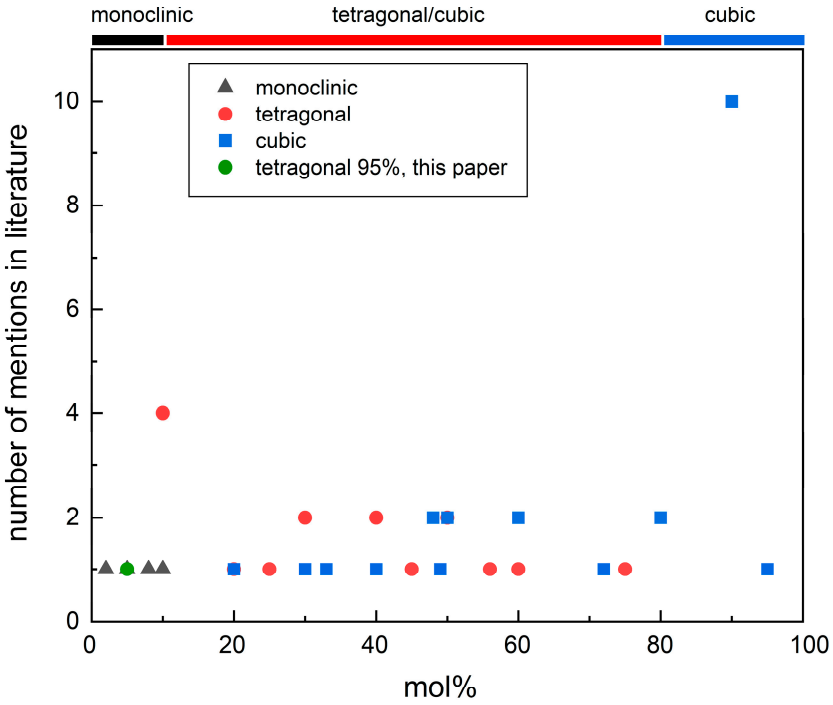

Figure 6. The histogram of phase distribution for ZrO_2 stabilized with mol% of CeO_2 evidenced in the different experimental studies and this paper (the *X*-axis shows the mol%, while the *Y*-axis shows the number of mentions of these structures).

The addition of CeO_2 results in a significant enhancement of the stability, high-temperature resistance, and mechanical properties of ZrO_2. In contrast, the higher amounts of CeO_2 enhance the mobility of grain boundaries and increase the grain size following sintering. Therefore, the CeO_2 addition should be minimized. As demonstrated in Figure 6, at low molar percentage values (below 8 mol%), the m-phase has thus far been achieved. The electroconsolidation method outlined in this study facilitates the production of a t-phase composite comprising only 5 mol% of CeO_2, a distinctive feature.

3.3. Strength Analysis

In Figure 7, there is an SEM image of a sintered sample fracture surface presented. It can be seen that after sintering, the grain size of around 1 μm was partially retained.

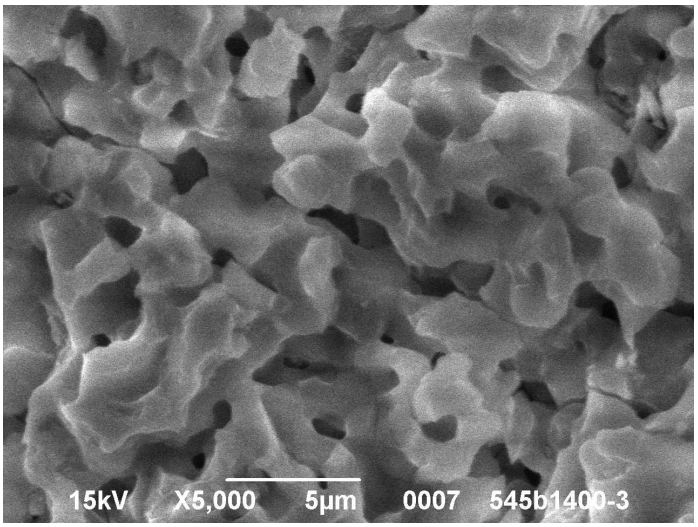

Figure 7. SEM image of a fracture surface of ZrO_2–5 wt.% CeO_2 sintered sample.

The destruction of grains observed in Figure 6 is predominantly transcrystalline, which indicates the strength of inter-grain boundaries. The bending strength σ_b of the specimen under three-point bending conditions was determined according to the following formula:

$$\sigma_b = \frac{3Fl}{2bh^2} \quad (1)$$

where F is the force value at the moment of separation of the sample into parts, N; l is the length of the sample, mm; b is the width of the sample, mm; h is the thickness of the sample in the parallel direction to the force applied to the sample, mm.

Different brittle materials experience rupture at different maximum tensile stresses. Statistically, the brittle fracture is dependent on the weakest element in the material's volume. According to the two-parameter Weibull distribution, the probability of failure P_f at a given the stress value, σ, is defined as follows [42,43]:

$$P_f = 1 - \exp\left[-\left(\frac{\sigma}{\sigma_0}\right)^m\right] \quad (2)$$

where m is the shape parameter of the Weibull distribution; σ is the actual inner stress under the applied force, MPa; and σ_0 denotes the scale parameter, MPa. (The threshold value, below which no specimen is expected to fail, is neglected).

To estimate the the Weibull parameters, Equation (1) is twice logarithmed and reduced to a linear form, as follows:

$$\ln\left(\ln\left(1 - P_f\right)^{-1}\right) = m\ln(\sigma) - m\ln(\sigma_0). \quad (3)$$

The shape and scale parameters, m and σ_0, respectively, are obtained from Equation (3) by the least squares method. The density of fracture probability f dependent on the value of σ_0 is described by the equation, as follows:

$$f(\sigma) = \frac{m}{\sigma_0}\left(\frac{\sigma}{\sigma_0}\right)^{m-1}\exp\left[-\left(\frac{\sigma}{\sigma_0}\right)^m\right] \quad (4)$$

To perform the calculations, the entered experimental data are ordered in ascending order, and for each i-th value, the empirical probability function $P_{exp}(i)$ is determined according to the following formula:

$$P_{exp}(i) = \frac{i - 0.5}{N}, \quad (5)$$

where N is the number of tested samples.

The results of the tensile strength measurement and of related calculations are collected in Table 2.

Table 2. Bending strength $\sigma = \sigma_f$ and the probability of failure P_f for the sintered samples of ZrO_2–5 wt.% CeO_2.

Experiment No.	σ_f, MPa	$\ln(\ln(1 - P_f)^{-1})$
1	370 ± 3	–3.218
2	390 ± 3	–2.355
3	400 ± 3	–2.068
4	420 ± 5	–1.349
5	430 ± 5	–1.061
6	440 ± 5	–0.630
7	446 ± 5	–0.486

Table 2. *Cont.*

Experiment No.	σ_f, MPa	$\ln(\ln(1-P_f)^{-1})$
8	450 ± 5	–0.342
9	454 ± 5	–0.198
10	460 ± 5	–0.054
11	476 ± 5	0.377
12	480 ± 5	0.521
13	484 ± 5	0.665
14	490 ± 5	0.809
15	494 ± 5	0.953

Using the obtained data, the Weibull graph, the so-called Weibull probability plot, was plotted and is presented in Figure 7. The values calculated from the experimental data were fitted using a linear equation, as follows:

$$y = a_0 x - a_1 \tag{6}$$

where the parameters a_0 and a_1 were determined using the least squares method. The Weibull modulus m corresponds to the parameter a_0.

The scale parameter σ_0 is related to both a_0 and a_1 according to the following relation:

$$\sigma_0 = \exp\left(\frac{a_1}{a_0}\right) \tag{7}$$

Figure 8 shows a Weibull graph, where $y = \ln(\ln(1-P_f)^{-1})$ represents the double logarithmic transformation of the cumulative probability of failure and $x = \ln(\sigma)$ describes the natural logarithm of the failure bending stress. The black dots correspond to the experimental data points. The linear regression model, fitted to the data points, yielded parameters describing the Weibull distribution listed in Table 3.

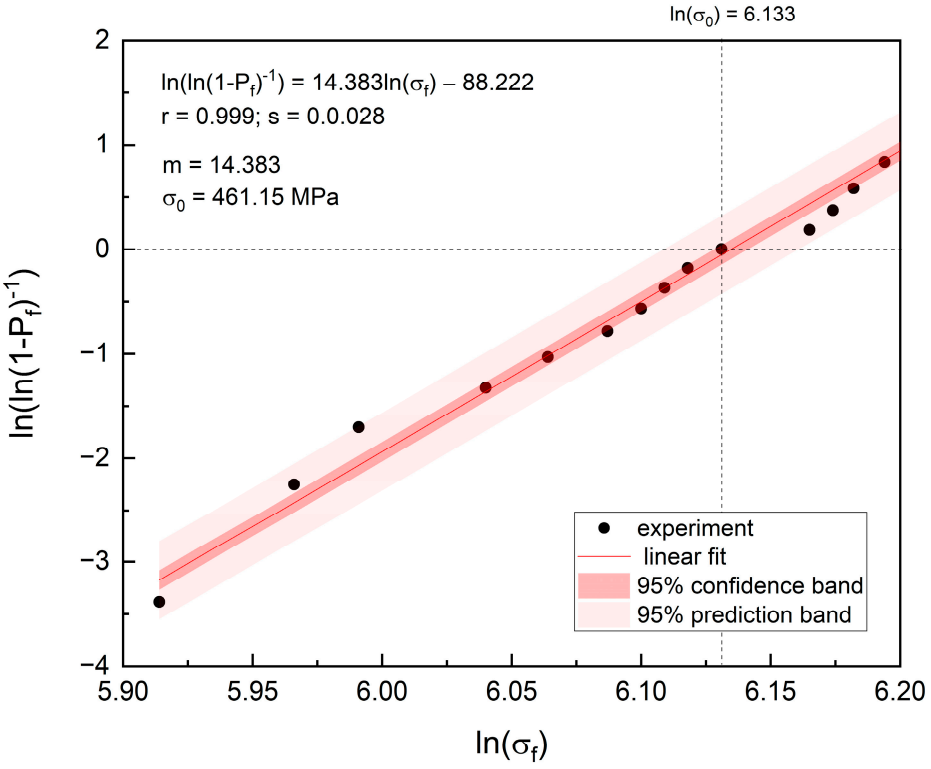

Figure 8. Weibull graph of the experimental bending strength for ZrO_2–5 wt.% CeO_2 sintered sample.

Table 3. The results of the parameter fitting for the best-fit formulation, along with the derived Weibull distribution parameters.

Fitting Parameters		Statistics of the Fit			Weibull Distribution Parameters	
a_0	a_1	r	s	Reduced χ^2	m	σ_0, MPa
$14.383 \pm 7.4 \times 10^{-6}$	$-88.222 \pm 1.36 \times 10^{-5}$	0.999	0.028	1.99×10^{-10}	$14.383 \pm 7.4 \times 10^{-6}$	$461.15 \pm 3.11 \times 10^{-5}$

It is noteworthy that the high Pearson's coefficient 0.999 and low curve fit standard deviation s = 0.28 of the experimental points from linearity suggest the high quality fit of the Weibull distribution.

The slope of the line is the shape parameter *m* of the Weibull distribution, the so-called modulus. Its positive value characterizes the curve as S-shaped with upward curvature followed by a turning (inflection) point. The m value of 14.383 indicates the variability of the material's strength. A relatively high Weibull modulus suggests a narrow flaw size population and, in a consequence, a narrow range of bending strengths.

The value of the Weibull modulus of the investigated sample is consistent with previously published studies [44,45]. Typically, zirconia ceramics are reported to exhibit a Weibull modulus below 7, while that of alumina ceramics can reach up to 10 [24]. However, there are reports demonstrating that the *m* values of the zirconia, both ZrO_2–Al_2O_3 microparticle and nanoparticle composites, were in a range between 10.07 and 12.02 [46]. In general, a higher Weibull modulus value represents a narrower dispersion of the fracture strength, and thus a more homogeneous distribution of flaws, providing higher reliability [46]. Thus, a high modulus suggests that the nanopowder studied is high quality and reliable.

The scale parameter σ_0 equal to 461.15 MPa is indicative of characteristic strength, representing the stress level at which 63.2% of the population would fail. Figure 8 reveals that the studied sample exhibits a high breakdown strength of 461.15 MPa.

The expected value to failure (mean value to failure) can be calculated based on the following equation:

$$MVF = \sigma\Gamma\left(1 + \frac{1}{m}\right) \quad (8)$$

where G is a gamma function. The average durability of the sample in terms of tensile strength measured by the expected value to failure is equal to 432.91 MPa. The median and mode are 449.54 and 461.08 MPa, respectively, and the standard deviation does not exceed 37.86 MPa, Table 4.

Table 4. The statistical parameters of the Weibull distribution of the experimental bending strength for ZrO_2–5 wt.% CeO_2 sintered sample.

Mean, MVF, MPa	Median, MPa	Mode, MPa	Standard Deviation, MPa
432.91	449.54	461.08	37.86

The mean and median values differ by 17 MPa. The median is a slightly more accurate estimator than the mean when the distribution is unsymmetrical.

The reliability function, which represents the probability that the sample will keep its properties without failure, and the failure function, which represents the probability of failure, are shown in Figure 9 (Both were plotted based on the parameters from the linear fit shown in Figure 8).

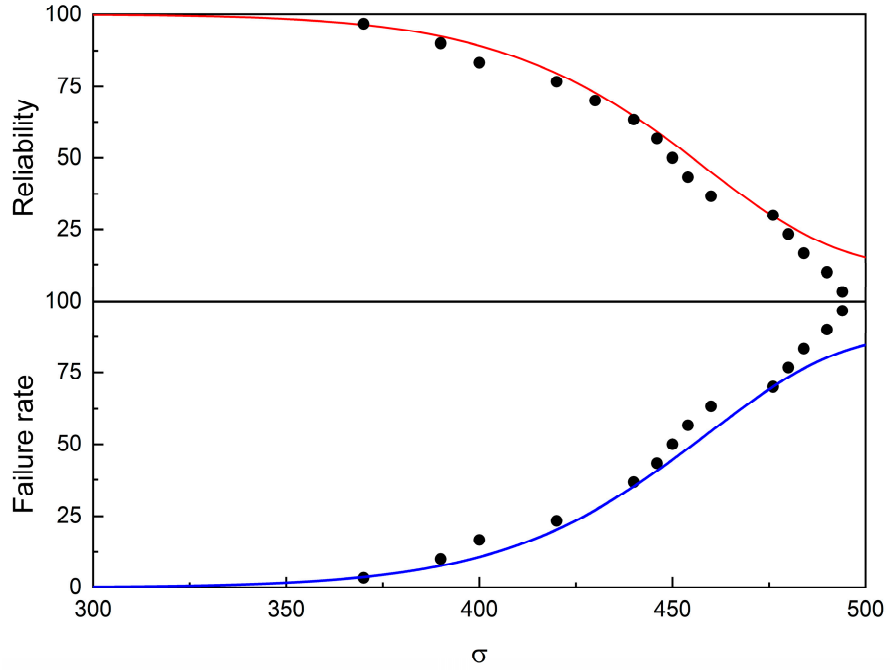

Figure 9. The reliability and failure functions drawn based on the parameters from the linear fit shown in Table 3 for the experimental bending strength for ZrO_2–5 wt.% CeO_2 sintered sample. The lines represent the model.

The hazard function, which describes the "conditional density", i.e., the conditional distribution of a random variable, given that the event has not yet occurred, and the failure distribution, i.e., the probability density of failures, are shown in Figure 10.

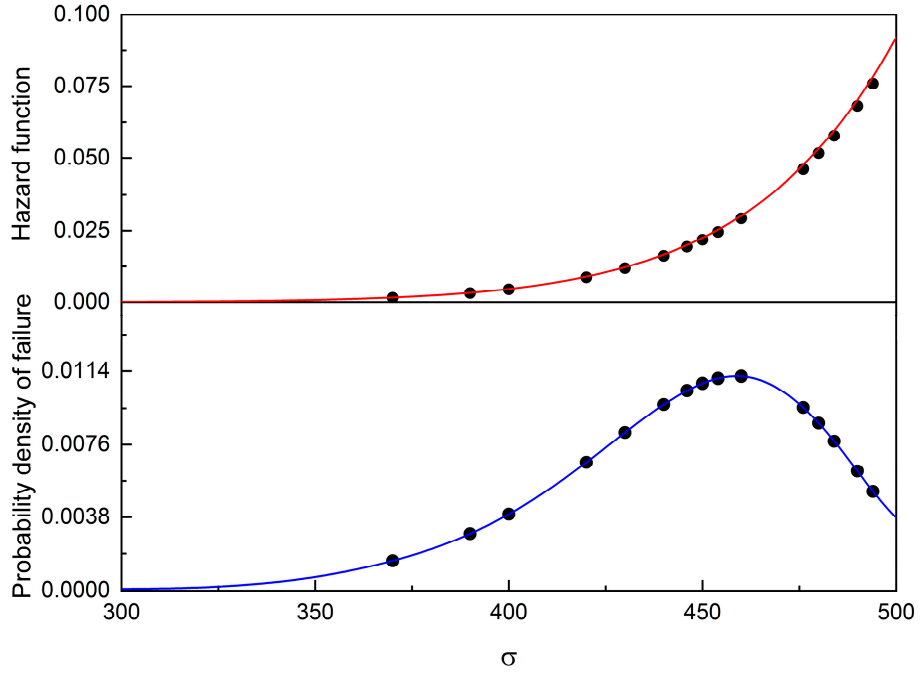

Figure 10. The hazard function (**top**) and probability density of failures (**bottom**) drawn based on the parameters from the linear fit shown in Table 3 for the experimental bending strength for ZrO_2–5 wt.% CeO_2 sintered sample. The black points on the graph illustrate only the experimental data, the σ values correspond to the experimental and hazard function (**top**) or probability density of failures (**bottom**); values are calculated based on the Weibull model.

An examination of the graphs shown in Figures 8 and 9 suggests that despite the high-quality fit, the scattering of the points from the Weibull model reveals a characteristic feature—splitting data into three groups. Well-defined groups of the points suggest that the Weibull model consists of three components as shown in Figure 11 and listed in Table 5.

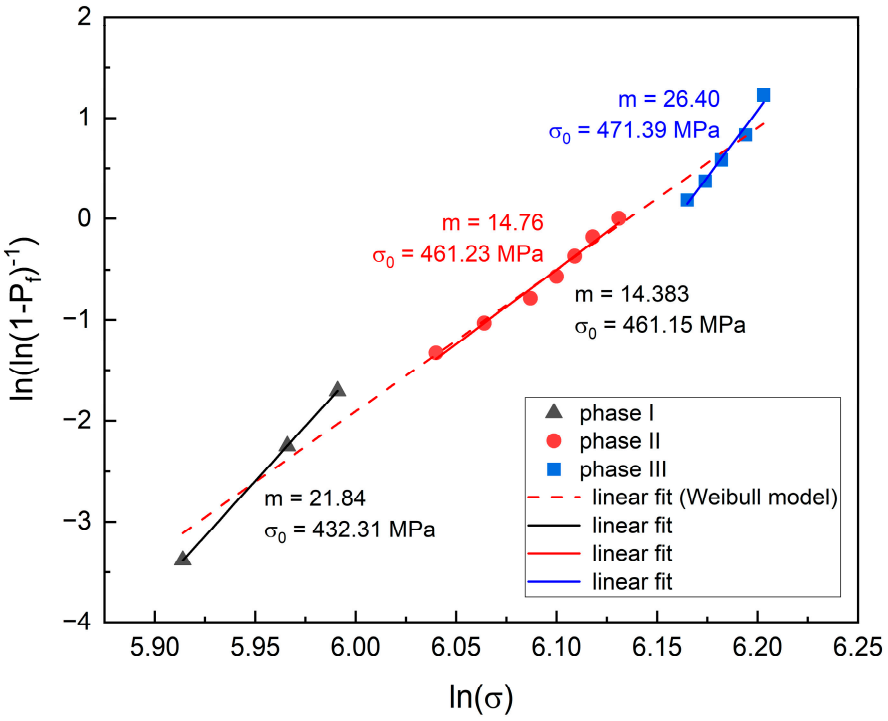

Figure 11. Three phases in the experimental bending strength for ZrO_2–5 wt.% CeO_2 sintered sample. The black triangles in the graph represent high content of m-phase, the red points represent mixture of m-phase and t-phase, and the blue squares represent high content of t-phase. The solid lines represent the linear fits, while the dashed line represents the linear fit of the total Weibull model.

Table 5. The results of the linear fitting of three phases, along with the Weibull distribution parameters.

Phase	Phase Content, %	Fit Parameters		Statistics of the Fit			Weibull Distribution Parameters		Δm *, deg	Median, GPa
		a_0	a_1	r	s	Reduced χ^2	m	σ_0, MPa		
I	3.1%	21.838 ± 0.027	−132.538 ± 0.162	1.000	0.0015	2.302×10^{-6}	21.84 ± 0.03	432.31 ± 0.19	1.356	425.12
II	92.5%	14.757 ± 0.845	−90.518 ± 5.149	0.992	0.0657	0.0043	14.76 ± 0.85	461.21 ± 7.49	0.100	449.90
III	4.4%	26.402 ± 2.195	−162.617 ± 13.573	0.989	0.0667	0.0045	26.40 ± 2.20	471.39 ± 15.58	1.808	464.89

* The difference between the slope of the total Weibull model and linear fit (phase I, II, or III) converted to degrees.

The slope of all three lines shown in Figure 11 is positive, but only the slope of the points in the middle part, shown in solid red, resembles those of the whole Weibull distribution (dashed line). The three lower points delineate phase I, the subsequent seven points delineate phase II, and the final five points delineate phase III. The Weibull modulus is different for each phase, Table 5. In the lower range, m is nearly 21.84, in the middle, it does not exceed 14.76, and in the upper range, it reaches 26.4. Although the differences in the m values may seem large, a comparison of the differences between the slope of the total Weibull model and each linear fit (phase I, II, or III) converted to degrees (inclination angles in degrees), Δm, shows that they are small. The percentages of phases are listed in the table. The characteristic strength values estimated based on these data are 432.31, 461.21, and 471.39 MPa, respectively. Thus, the three lower points (370, 390, and 400) reveal a greater influence of the m-phase, seven points in the middle of the graph reveal a mixture of the m-phase and t-phase, and the upper five (476, 480, 484, 490, and 494) reveal the larger influence of the t-phase. In each of them, the Weibull modulus is slightly different, the

highest for the upper and the smallest for the middle part. The variation in the Weibull distribution parameters seems to be related to the temperature gradient during sintering, which in turn is related to the grain size.

3.4. Hardness Analysis

The procedure previously described was employed once more in order to analyze the distribution of the values of hardness. The results of the Vickers hardness measurement are collected in Table 6.

Table 6. Vickers hardness results and parameters of the Weibull distribution for the sintered samples of ZrO_2–5 wt.% CeO_2.

Experiment No.	HV_{10}, GPa	$\ln(\ln(1-P_f)^{-1})$
1	17.5 ± 0.5	−3.218
2	18.2 ± 0.5	−2.355
3	18.65 ± 0.5	−2.068
4	19.2 ± 0.5	−1.349
5	19.32 ± 0.5	–1.061
6	20.2 ± 0.5	–0.630
7	20.35 ± 0.5	–0.486
8	20.65 ± 0.5	–0.342
9	21.55 ± 0.5	–0.198
10	21.8 ± 0.5	–0.054
11	22.2 ± 0.5	0.377
12	22.5 ± 0.5	0.521
13	22.55 ± 0.5	0.665
14	23.2 ± 0.5	0.809
15	23.25 ± 0.5	0.953

Figure 12 shows a Weibull graph, where $y = \ln(\ln(1-P_f)^{-1})$ represents the double logarithmic transformation of the cumulative probability of failure and $x = \ln(HV_{10})$ describes the natural logarithm of the failure of Vicker hardness. The black dots correspond to the experimental data points. The linear regression model, fitted to the data points, yielded the parameters describing the Weibull distribution listed in Table 7.

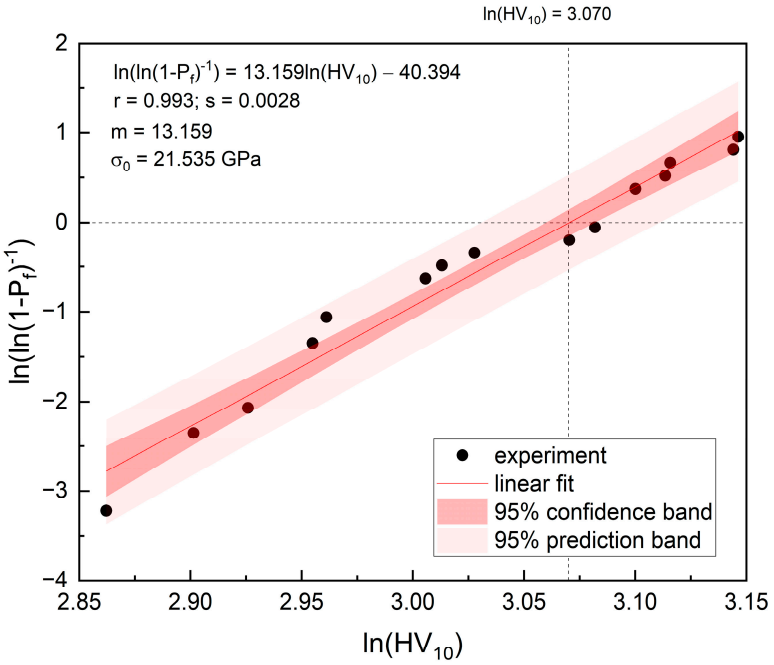

Figure 12. Weibull distribution of the hardness for ZrO_2–5 wt.% CeO_2 sintered sample.

Table 7. The parameters of the Weibull distribution of the hardness for ZrO_2–5 wt.% CeO_2 sintered sample.

Fit Parameters		Statistics of the Fit			Weibull Distribution Parameters	
a_0	a_1	r	s	Reduced χ^2	m	HV_{10}, GPa
$13.159 \pm 3.43 \times 10^{-6}$	-40.394 ± 2.092	0.999	0.0052	1.14×10^{-14}	$13.159 \pm 3.43 \times 10^{-6}$	$21.535 \pm 4.21 \times 10^{-6}$

The relatively high Weibull modulus, *m*, of 13.159 suggests a narrow range of the hardness values, indicating a constant material hardness. The scale parameter σ_0, that does not exceed 21.535 GPa, is the characteristic hardness value reached or exceeded by as much as 63.2% of the population. The value of the Weibull modulus of 13.159 GPa is consistent with results obtained from the bending strength analysis presented in Section 3.3 and with those published in other reports [44–46].

The expected value to failure (mean value to failure) was calculated based on Equation (8). The average durability of the sample in terms of hardness measured by the expected value to failure is equal to 20.079 GPa, Table 8.

Table 8. The statistical parameters of the Weibull distribution of the hardness for ZrO_2–5 wt.% CeO_2 sintered sample.

Mean, GPa	Median, GPa	Mode, GPa	Standard Deviation, GPa
20.079	20.943	21.456	1.919

The median and the mean are almost identical, suggesting a moderately symmetrical distribution. The reliability function (the probability that the sample will keep its properties without failure) as well as failure function (the probability of failure) are shown in Figure 13. (Both were plotted based on the parameters from the linear fit shown in Figure 12).

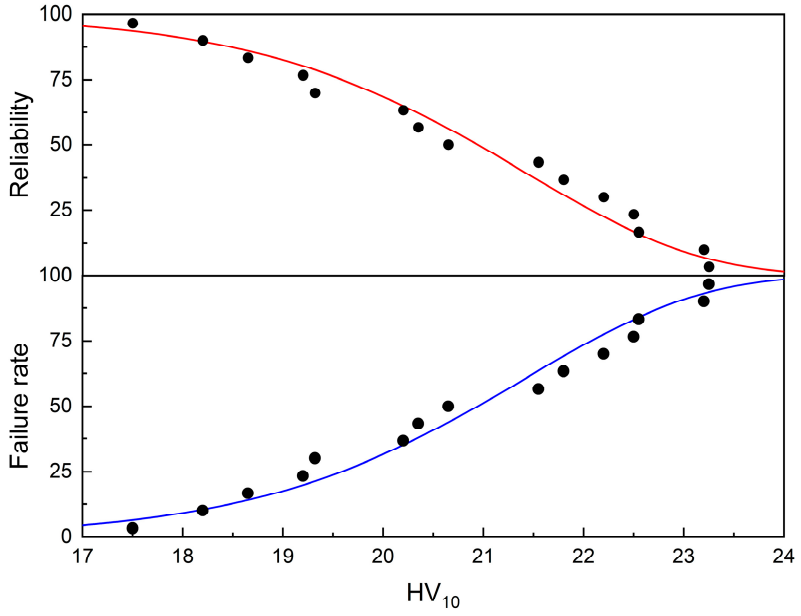

Figure 13. The reliability and failure functions drawn based on the parameters from the linear fit shown in Table 7 for the experimental hardness for ZrO_2–5 wt.% CeO_2 sintered sample. The black points on the graph represent experimental data, whilst the solid lines represent the Weibull model.

The failure function, widely known as the hazard rate, and the probability density of failure are shown in Figure 14.

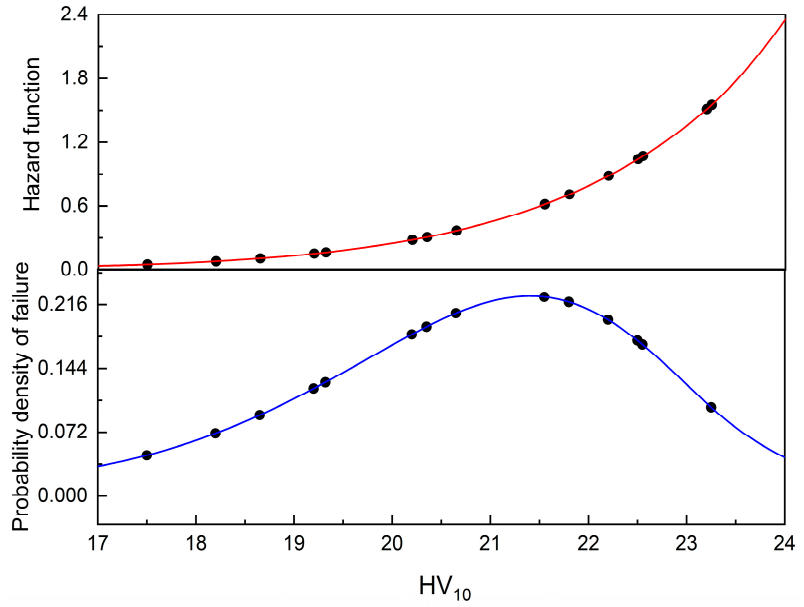

Figure 14. The hazard and probability density of failures functions drawn based on the parameters from the linear fit parameters from Table 7 for the experimental hardness for ZrO_2–5 wt.% CeO_2 sintered sample; the solid lines represent the Weibull model. The black points on the graph illustrate only the experimental data, the σ values corresponding to the experimental and hazard function (**top**) or probability density of failures (**bottom**) values are calculated based on the Weibull model.

A thorough analysis of the data from the Weibull model depicted in Figure 12 reveals the presence of three distinct groups in the distribution. This indicates the Weibull model comprises three components, as illustrated in Figure 15 and listed in Table 9.

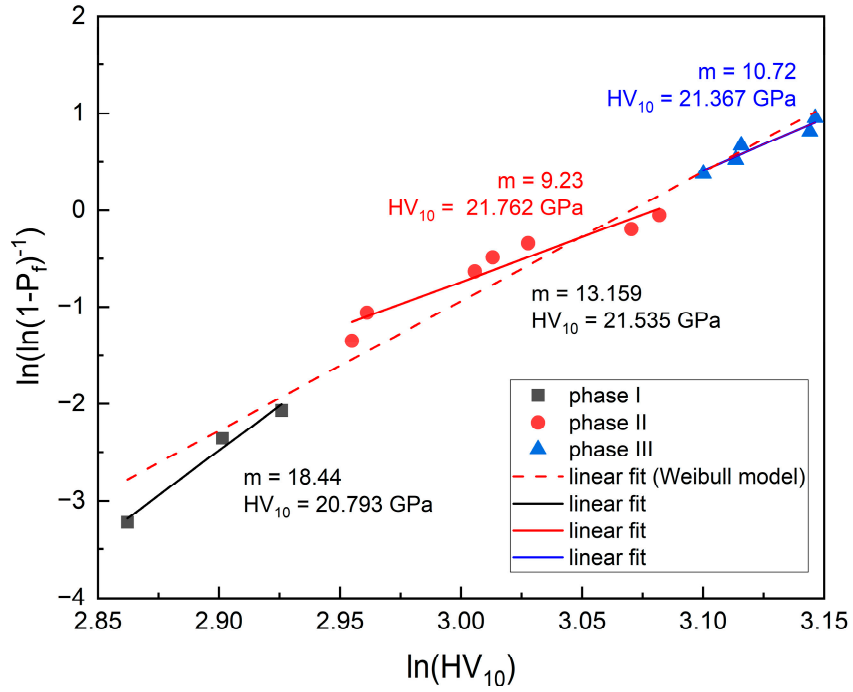

Figure 15. Three phases in the experimental hardness for ZrO_2–5 wt.% CeO_2 sintered sample. The black triangles in the graph represent high content of m-phase, the red points represent mixture of m-phase and t-phase, and the blue squares represent high content of t-phase. The solid lines represent linear fit and dashed line the total Weibull model.

Table 9. The results of the linear fitting of three regions, along with the derived Weibull distribution parameters.

Phase	Phase Content, %	Fitting Parameters		Statistics of the Fit			Weibull Distribution Parameters		Δm * [deg]	Median
		a_0	a_1	r	s	Reduced χ^2	m	HV_{10}, GPa		
I	0.5%	18.438 ± 2.75	−55.952 ± 7.967	0.9782	0.125	0.0156	18.438 ± 2.75	20.793 ± 3.38	1.24	20.384
II	99.1%	9.225 ± 1.161	−28.415 ± 3.502	0.9626	0.138	0.0193	9.225 ± 1.161	21.762 ± 4.19	−1.84	21.648
III	0.4%	10.718 ± 1.875	−32.817 ± 5.856	0.9159	0.076	0.0058	10.718 ± 1.875	21.367 ± 6.77	−0.98	20.648

* The difference between the slope of the total Weibull model and linear fit (phase I, II, or III) converted to degrees.

Figure 15 shows that all three lines have a positive slope, but only the blue points at the top match the whole dataset slope (dashed line). Thus, the Weibull model describes in fact three different distributions. The three lower points delineate phase I, the subsequent seven points delineate phase II, and the final five points delineate phase III. The Weibull modulus is different in each phase, Table 9. In the lower range, m is almost 18.44, in the middle, it does not exceed 9.23, and in the upper range, it reaches 10.72. Although the differences in the m values may seem large, a comparison of the differences between the slope of the total Weibull model and each linear fit (phase I, II, or III) converted to degrees (inclination angles in degrees), Δm, shows that they are small. The percentages of the phases are listed in the table. The characteristic hardnesses estimated based on these data are equal to 20.703, 21.762, and 21.367 GPa, respectively. Thus, the three lower points (370, 390, and 400; depicted in black) reveal a negligible influence of the m-phase, which has lower symmetry. The seven points in the middle of the graph (depicted in red) reveal a mixture of the m-phase and t-phase, and the top five (476, 480, 484, 490, and 494; depicted in blue) reveal a negligible influence of the t-phase. The difference between the hardness in the phases I, II, and III is negligible. Thus, the hardness is very stable.

The Weibull modulus, when greater than 4, is indicative of the inherent property limitations of materials, e.g., ceramic brittleness. However, it also is indicative of severe problems in the manufacturing process, or of minor variability in the manufacturing process or in the material itself. The results obtained indicate a high homogeneity of the material tested, not only as regards strength but also hardness. Thus, the high values of the Weibull modulus suggest that the nanopowder studied is high quality and reliable in terms of hardness and strength.

4. Conclusions

From the performed experiments and statistical analysis of the results, the following conclusions can be derived. The high value of shape parameter m = 14.383 indicated that the bending strength of ZrO_2 stabilized with 5 wt.% CeO_2 samples exhibited low variability. This result suggested consistent material performance. The characteristic strength σ_0 = 461.15 MPa was relatively high, which proved that the material could withstand substantial stress before failure.

The linearity of the plot shows a good fit to the Weibull distribution, suggesting that the model was appropriate for prediction of the probability of failure under respective loads. The small scattering of the experimental points from the straight line indicates the high quality and repeatability of the manufacturing process, and subsequent uniformity of the material properties.

The high value of the shape parameter indicates the uniformity and repeatability of the hardness reached by the fabricated specimens. A scale parameter of σ_0 = 21.535 GPa suggests the material can maintain high hardness levels under typical work conditions. Based on the hardness and strength Weibull distribution analysis, it can be concluded that the proper quality of ZrO_2–5 wt.% CeO_2 was reached and can be kept in the subsequent stages

of the research program on the electroconsolidation process. In particular, the analysis provided a solid ground for preparation of the modified, improved device prototype.

It appears that the variability of the Weibull distribution parameters is associated with the temperature gradient during the process of sintering. The experimental evidence and statistical analysis reveal an influence of the m-phase, which has lower symmetry and, therefore, its addition make ceramic weaker and softer. Furthermore, their progressive replacement by the t-phase, which has higher symmetry, makes ceramic both harder and stronger. Reducing the mol% increases the risk of the appearance of the highest addition of the monoclinic phase; increasing it is unfavorable from the point of view of the sintering process. Statistical and manufacturing evidence suggests that the choice of 5%/mol is optimal.

The results of the research demonstrated that the sintered specimens sintered with a novel electroconsolidation method out of ceria-stabilized zirconia powder exhibited high strength and retained high hardness. Repeatable sintering conditions and the addition of 5 mol% CeO_2 ensured the reproducibility of the high-quality properties of the tested ceramic. They reveal the high sensitivity of the nanopowders (their structure and grain size) to the temperature gradient.

Further improvement can be reached through optimization of the synthesis route, modification of the ceria content, and experiments with altered sintering conditions. In particular, it could be expected that improved structural homogeneity and nanoscale features might be reached through optimal heating rate control, related to the respective phases of the sintering process. Works on further improvement of the electroconsolidation process and respective zirconia-based ceramics' properties and reproducibility are planned.

Author Contributions: Conceptualization, E.H., D.M. and J.M.; methodology, M.R., E.H., V.K., T.R. and J.N.L.; software, L.C., T.R. and J.N.L.; validation, W.S., J.M., M.R. and T.R.; formal analysis, M.R., V.K., L.C., J.M. and J.N.L.; investigation, E.H., V.K. and M.M.; resources, E.H. and D.M.; data curation, L.C.; writing—original draft preparation, M.R.; writing—review and editing, all authors; visualization, V.K., D.M., M.M. and J.N.L.; supervision, M.R. and W.S.; project administration, W.S.; funding acquisition, M.M. All authors have read and agreed to the published version of the manuscript.

Funding: The research was financed by the National Science Centre, Poland, project No. 2022/47/B/ST5/01041. Milan Masař would like to acknowledge funding from the Centre of Polymer Systems Development Project No. RP/CPS/2024-28/007.

Institutional Review Board Statement: Not applicable.

Informed Consent Statement: Not applicable.

Data Availability Statement: The raw data supporting the conclusions of this article will be made available by the authors on request.

Acknowledgments: The authors express their gratitude to D. Sofronov (State Scientific Institution Institute for Single Crystals, National Academy of Sciences of Ukraine) for the kind support and excellent materials for the experiments.

Conflicts of Interest: The authors declare no conflicts of interest.

References

1. Raj, R.; Singh, G. A review on process prerequisites and biomedical applications of additively manufactured zirconia. *Eng. Sci. Technol. Int. J.* **2024**, *59*, 101876. [CrossRef]
2. Cesar, P.F.; Miranda, R.B.D.P.; Santos, K.F.; Scherrer, S.S.; Zhang, Y. Recent advances in dental zirconia: 15 years of material and processing evolution. *Dent. Mater.* **2024**, *40*, 824–836. [CrossRef]

3. Sun, Y.; Ma, L.; Jia, J.; Tan, Y.; Qi, S.; Tang, B.; Li, H.; Zhou, Y. The generation mechanism of cutting heat and the theoretical prediction model for temperature on the rake face of the cutting tool in Zirconia ceramics. *J. Manuf. Process.* **2024**, *132*, 584–597. [CrossRef]
4. Liu, X.M. The influence of cerium oxide content on the crack growth in zirconia ceramic materials for engineering applications. *Results Mater.* **2021**, *10*, 100196. [CrossRef]
5. Gasparetto, H.; Salau, N.P.G. A review on ethanol steam reforming focusing on yttria-stabilized zirconia catalysts: A look into hydrogen production for fuel cells. *Fuel* **2024**, *371 Pt B*, 132140. [CrossRef]
6. Zhu, M.; Zhang, P.; Gao, F.; Bai, Y.; Zhang, H.; Zu, M.; Liu, L.; Zhang, Z. Advanced lightweight lightning strike protection composites based on super-aligned carbon nanotube films and thermal-resistant zirconia fibers. *Nanoscale Adv.* **2024**, *6*, 4858–4864. [CrossRef]
7. Lityagina, L.M.; Kabalkina, S.S.; Pashkina, T.A.; Khzyainov, A. Polymorphism of ZrO_2 at high pressures. *Sov. Phys. Solid State* **1978**, *20*, 2009.
8. Liu, L. New high pressure phases of ZrO_2 and HfO_2. *J. Phys. Chem. Solids* **1980**, *41*, 331–334. [CrossRef]
9. Leger, J.M.; Atouf, A.; Tomaszewski, P.E.; Pereira, A.S. Pressure-induced structural phase transitions in zirconia under high pressure. *Phys. Rev. B* **1993**, *47*, 14075. [CrossRef]
10. Affatato, S.; Grillini, L. Topography in bio-tribocorrosion. In *Bio-Tribocorrosion in Biomaterials and Medical Implants*; Yan, Y., Ed.; Woodhead Publishing: Cambridge, UK, 2013; pp. 1a–22a. [CrossRef]
11. King, A. *Critical Materials*; Elsevier: Amsterdam, The Netherlands, 2021; pp. 205–234. [CrossRef]
12. Liens, A.; Reveron, H.; Douillard, T.; Blanchard, N.; Lughi, V.; Sergo, V.; Laquai, R.; Müller, B.R.; Bruno, G.; Schomer, S.; et al. Phase transformation induces plasticity with negligible damage in ceria-stabilized zirconia-based ceramics. *Acta Mater.* **2020**, *183*, 261–273. [CrossRef]
13. Tzanakakis, E.; Kontonasaki, E.; Tzoutzas, I. Zirconia: Contemporary views of a much talked material: Structure, applications and clinical considerations. *Hell. Stomatol. Rev.* **2013**, *57*, 101–137.
14. Li, Z.; Wu, J.; Luo, J.; Zhang, B.; Li, Y.; Cheng, B.; Yang, J.; Li, B.; Wang, X. Effects of Alumina Modification on Curing Performance of Ceria-stabilized Zirconia in Stereolithography. *J. Alloys Compd.* **2025**, *1012*, 178438. [CrossRef]
15. Gómez, S.; Suárez, G.; Rendtorff, N.M.; Aglietti, E.F. Relation between mechanical and textural properties of dense materials of tetragonal and cubic zirconia. *Sci. Sinter.* **2016**, *48*, 119–130. [CrossRef]
16. Jagdale, G.S.; Choi, M.H.; Siepser, N.P.; Jeong, S.; Wang, Y.; Skalla, R.X.; Huang, K.; Ye, X.; Baker, L.A. Electrospray deposition for single nanoparticle studies. *Anal. Methods* **2021**, *13*, 4105–4113. [CrossRef]
17. Burk, R.C.; Zawidzki, T.W.; Apte, P.S. Particle Size Distribution and Its Relation to Sintering—A Case Study for UO_2 Powders. *J. Am. Ceram. Soc.* **1983**, *66*, 815–818. [CrossRef]
18. Daassi, R.; Durand, K.; Rodrigue, D.; Stevanovic, T. Optimization of the Electrospray Process to Produce Lignin Nanoparticles for PLA-Based Food Packaging. *Polymers* **2023**, *15*, 2973. [CrossRef]
19. Struz, J.; Hruzik, L.; Klapetek, L.; Trochta, M. Comparative analysis of different softwares in terms of parameters optimized by topological optimization. *MM Sci. J.* **2023**, 6346–6353. [CrossRef]
20. Hevorkian, E.; Jozwik, J.; Rucki, M.; Kolodnitskyi, V.; Morozova, O.; Dziedzic, K. Reproducibility of Properties of the Zirconia-Based Composites. In Proceedings of the 11th International Workshop on Metrology for AeroSpace (MetroAeroSpace), Lublin, Poland, 3–5 June 2024; pp. 484–489. [CrossRef]
21. Silva, J.; Vaz, P.; Martins, P.; Ferreira, L. Reliability Estimation Using EM Algorithm with Censored Data: A Case Study on Centrifugal Pumps in an Oil Refinery. *Appl. Sci.* **2023**, *13*, 7736. [CrossRef]
22. Dong, X.; Sun, F.; Xu, F.; Zhang, Q.; Zhou, R.; Zhang, L.; Liang, Z. Three-Parameter Estimation Method of Multiple Hybrid Weibull Distribution Based on the EM Optimization Algorithm. *Mathematics* **2022**, *10*, 4337. [CrossRef]
23. Lei, W.S.; Yu, Z.S.; Zhang, P.; Qian, G. Standardized Weibull statistics of ceramic strength. *Ceram. Int.* **2021**, *47*, 4972–4993. [CrossRef]
24. Osuchukwu, O.A.; Salihi, A.; Ibrahim, A.; Audu, A.A.; Makoyo, M.; Mohammed, S.A.; Lawal, M.Y.; Etinosa, P.O.; Isaac, I.O.; Oni, P.G.; et al. Weibull analysis of ceramics and related materials: A review. *Heliyon* **2024**, *10*, e32495. [CrossRef] [PubMed]
25. Barbosa, L.A.P.; Gerke, K.M.; Munkholm, L.J.; Keller, T.; Gerke, H.H. Discrete element modeling of aggregate shape and internal structure effects on Weibull distribution of tensile strength. *Soil Tillage Res.* **2022**, *219*, 105341. [CrossRef]
26. Teixeira, L.B.; de Moraes, E.G.; de Oliveira, A.P.N. Influence of single-side ion exchange parameters in LZS and LZSA sintered glass-ceramics. *Boletín Soc. Esp. Cerám. Vidr.* **2022**, *61*, 663–676. [CrossRef]
27. Bernal, R.A. On the application of Weibull statistics for describing strength of micro and nanostructures. *Mech. Mater.* **2021**, *162*, 104057. [CrossRef]
28. Zhou, D.; Chen, D.; Yang, F.; Mei, J.; Yao, Y.; Deng, Y. Freeze–thaw damage analysis and life prediction of modified pervious concrete based on Weibull distribution. *Case Stud. Constr. Mater.* **2024**, *20*, e03305. [CrossRef]

29. Hevorkian, E.; Michalczewski, R.; Rucki, M.; Sofronov, D.; Osuch-Słomka, E.; Nerubatskyi, V.; Krzysiak, Z.; Latosińska, J.N. Effect of the sintering parameters on the structure and mechanical properties of zirconia-based ceramics. *Ceram. Int.* **2024**, *50 Pt A*, 35226–35235. [CrossRef]
30. Prakasam, M.; Valsan, S.; Lu, Y.; Balima, F.; Lu, W.; Piticescu, R.; Largeteau, A. Nanostructured Pure and Doped Zirconia: Synthesis and Sintering for SOFC and Optical Applications. In *Sintering Technology: Method and Application*; InTechOpen: Rijeka, Croatia, 2018. [CrossRef]
31. Pandey, A.K.; Biswas, K. Influence of sintering parameters on tribological properties of ceria stabilized zirconia bio-ceramics. *Ceram. Int.* **2011**, *37*, 257–264. [CrossRef]
32. Sainz, M.A.; Serena, S.; Caballero, A. Synthesis and properties of Zn and Zn–Mg-doped tricalcium phosphates obtained by Spark Plasma Sintering. *Ceram. Int.* **2023**, *49*, 19569–19577. [CrossRef]
33. Ma, L.Y.; Wan, M.; Zhang, Z.Y.; Meng, B. Effect of sintering duration on microstructure and properties of Inconel 718 superalloy prepared by electric field-activated sintering. *J. Manuf. Process.* **2023**, *105*, 27–37. [CrossRef]
34. Hevorkian, E.S.; Nerubatskyi, V.P.; Rucki, M.; Kilikevicius, A.; Mamalis, A.G.; Samociuk, W.; Morozow, D. Electroconsolidation Method for Fabrication of Fine-Dispersed High-Density Ceramics. *Nanotechnol. Percept.* **2024**, *20*, 100–113.
35. Ralls, A.M.; Daroonparvar, M.; Menezes, P.L. Spark Plasma Sintering of Mg-based Alloys: Microstructure, Mechanical Properties, Corrosion Behavior, and Tribological Performance. *J. Magnes. Alloys* **2024**, *12*, 405–442. [CrossRef]
36. Cychosz, K.A.; Thommes, M. Progress in the Physisorption Characterization of Nanoporous Gas Storage Materials. *Engineering* **2018**, *4*, 559–566. [CrossRef]
37. Yang, Y.; Li, W.; Tang, W.; Li, B.; Zhang, D. Sample Sizes Based on Weibull Distribution and Normal Distribution for FRP Tensile Coupon Test. *Materials* **2019**, *12*, 126. [CrossRef]
38. Chang, H.J.; Huang, K.C.; Wu, C.X. Determination of Sample Size in Using Central Limit Theorem for Weibull Distribution. *Int. J. Inf. Manag. Sci.* **2006**, *17*, 31–46.
39. Fernández, A.J. Tolerance Limits and Sample-Size Determination Using Weibull Trimmed Data. *Axioms* **2023**, *12*, 351. [CrossRef]
40. Thommes, M.; Kaneko, K.; Neimark, A.V.; Olivier, J.P.; Rodriguez-Reinoso, F.; Rouquerol, J.; Sing, K.S.W. Physisorption of gases, with special reference to the evaluation of surface area and pore size distribution (IUPAC technical report). *Pure Appl. Chem.* **2015**, *87*, 1051–1069. [CrossRef]
41. Krzysiak, Z.; Gevorkyan, E.; Nerubatskyi, V.; Rucki, M.; Chyshkala, V.; Caban, J.; Mazur, T. Peculiarities of the Phase Formation during Electroconsolidation of Al_2O_3–SiO_2–ZrO_2 Powders Mixtures. *Materials* **2022**, *15*, 6073. [CrossRef]
42. Wang, L.; Jiao, Y.; Yao, L.; Sheng, Y.; Hao, Z.; Tang, W.; Dou, R. Investigation of mechanical properties and low-temperature degradation of dental 3Y-TZP ceramics fabricated by stereolithography in combination with microwave sintering. *J. Mech. Behav. Biomed. Mater.* **2023**, *148*, 106211. [CrossRef]
43. Hatanaka, G.R.; Polli, G.S.; Adabo, G.L. The mechanical behavior of high-translucent monolithic zirconia after adjustment and finishing procedures and artificial aging. *J. Prosthet. Dent.* **2020**, *123*, 330–337. [CrossRef]
44. Strazzi-Sahyon, H.B.; Campos, T.M.B.; dos Santos, C.; Piza, M.M.T.; Alves, L.M.M.; Benalcazar Jalkh, E.B.; Bergamo, E.T.P.; Tebcherani, S.M.; Witek, L.; Coelho, P.G.; et al. Effect of calcination on minimally processed recycled zirconia powder derived from milling waste. *Dent. Mater.* **2024**, *40*, 1477–1486. [CrossRef]
45. Wirwicki, M.; Lichołai, L.; Dębska, B.; Miąsik, P.; Szyszka, J.; Krasoń, J.; Szalacha, A. Two-parametric analysis of the Weibull distribution strength of advanced ceramics materials. *E3S Web Conf.* **2018**, *49*, 00130. [CrossRef]
46. Seo, J.Y.; Oh, D.; Kim, D.J.; Kim, K.M.; Kwon, J.S. Enhanced mechanical properties of ZrO_2-Al_2O_3 dental ceramic composites by altering Al_2O_3 form. *Dent. Mater.* **2020**, *36*, e117–e125. [CrossRef] [PubMed]